HHS Public Access

Author manuscript

J Med Chem. Author manuscript; available in PMC 2022 March 11.

Published in final edited form as:

J Med Chem. 2021 March 11; 64(5): 2691–2704. doi:10.1021/acs.jmedchem.0c01922.

A Unique Molecular Interaction with Histone Deacetylase 6 Catalytic Tunnel: Crystallographic and Biological Characterization of a Model Chemotype

Olasunkanmi O. Olaoye[a,b], **Paris R. Watson**[c], **Nabanita Nawar**[a,b], **Mulu Geletu**[a], **Abootaleb Sedighi**[a], **Shazreh Bukhari**[a,b], **Yasir S. Raouf**[a,b], **Pimyupa Manaswiyoungkul**[a,b], **Fettah Erdogan**[a,b], **Ayah Abdeldayem**[a,b], **Aaron D. Cabral**[a,b], **Muhammad Murtaza Hassan**[a,b], **Krimo Toutah**[a], **Andrew E. Shouksmith**[a], **Justyna M. Gawel**[a], **Johan Israelian**[a,b], **Tudor B. Radu**[a,b], **Niyati Kachhiyapatel**[a], **Elvin D. de Araujo**[a], **David W. Christianson**[c,*], **Patrick T. Gunning**[a,b,*]

[a]Department of Chemical and Physical Sciences, University of Toronto Mississauga, 3359 Mississauga Rd N., Mississauga, Ontario L5L 1C6, Canada

[b]Department of Chemistry, University of Toronto, 80 St. George Street, Toronto, Ontario M5S 3H6, Canada

[c]Roy and Diana Vagelos Laboratories, Department of Chemistry, University of Pennsylvania, 231 South 34th Street, Philadelphia, PA 19104-6323, United States

Abstract

HDAC6 is involved in multiple regulatory processes, ranging from cellular stress to intracellular transport. Inhibition of aberrant HDAC6 activity in several cancers and neurological diseases has

[*]**Corresponding Author:** Correspondence should be directed to David W. Christianson and Patrick T. Gunning, Patrick T. Gunning, Department of Chemical and Physical Sciences, University of Toronto Mississauga, 3359 Mississauga Rd N., Mississauga, Ontario, Canada. patrick.gunning@utoronto.ca, David W. Christianson, Roy and Diana Vagelos Laboratories, Department of Chemistry, University of Pennsylvania, 231 South 34th Street, Philadelphia, PA 19104-6323, United States. chris@sas.upenn.edu.

Author Contributions

O.O.O., A.E.S., K.T., E.D.A., and P.T.G. designed this study. O.O.O., E.D.A., P.R.W., D.W.C., and P.T.G. drafted the manuscript. O.O.O. synthesized the chemical compounds. P.R.W. and D.W.C. performed the x-ray crystallography studies, data collection and x-ray structure analysis. N.N., M.G., S.B., P.M., A.D.C., J.M.G, and A.A. conducted the cellular biology and biophysical experiments. Y.R. and O.O.O. carried out the *in-silico* docking simulations. A.S., T.B.R., and J.I. conducted the PAMPA, plasma, blood stability, and toxicity assays. O.O.O., F.E., M.M.H., N.K., and E.D.A. expressed and purified the recombinant protein used for biophysical studies.

Supporting Information

The supporting information is available free of charge at:

HDAC binding and inhibition profiles using fluorescence polarization and enzymatic activity assays; PAMPA, kinetic solubility, and pharmacokinetic data; cell population sorting; cell viability screens; mass spectrometry; immunofluorescence; synthetic schemes, experimental procedures and compound characterization (PDF)

Molecular formula strings (CSV)

Docking of TO-317 with drHDAC6 (PDB)

Docking of 1 with drHDAC6 (PDB)

Docking of 2 with drHDAC6 (PDB)

Docking of Citarinostat with drHDAC6 (PDB)

Docking of TO-317 with HDAC8 (PDB)

Data Availability

Atomic coordinates and structure factor amplitudes for the drHDAC6-**TO-317** complex are deposited in the Protein Data Bank (www.rcsb.org) with accession code **7JOM**.

Authors will release the atomic coordinates and experimental data upon article publication.

Competing Interests

The authors declare no competing interests.

been shown to be efficacious in both preclinical and clinical studies. While selective HDAC6-targeting has been pursued as an alternative to pan-HDAC drugs, identifying truly selective molecular templates has not been trivial. Herein, we report an SAR study yielding **TO-317**, which potently binds the HDAC6 catalytic domain 2 (K_i = 0.7 nM) and inhibits enzyme function (IC_{50} = 2 nM). **TO-317** exhibits 158-fold selectivity for HDAC6 over other HDAC isozymes by binding the catalytic Zn^{2+} and, uniquely, making a never seen before, direct hydrogen bond with the Zn^{2+} coordinating residue, His614. This novel structural motif targeting the second sphere His614 interaction, observed in a 1.84 Å-resolution crystal structure with *dr*HDAC6 from zebrafish, can provide new pharmacophores for identifying enthalpically driven, high affinity, HDAC6-selective inhibitors

Graphical Abstract

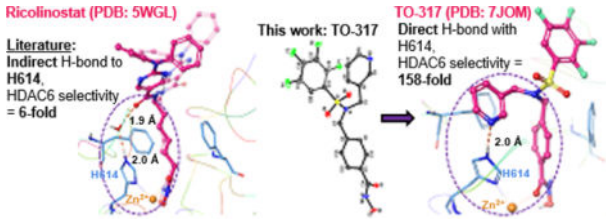

Introduction

Histone Deacetylases (HDACs) are widely investigated as clinical targets due to their role as epigenetic modulators.[1–6] There are 18 known HDACs, with 11 having Zn^{2+}-dependent catalytic deacetylation activity, and the remaining 7, referred to as sirtuins (Class III HDACs), exhibiting NAD^+-dependent deacetylation. The 11 Zn^{2+}-dependent HDACs are further differentiated into four distinct classes, based on phylogenetic analysis.[7,8] HDACs 1, 2, 3, and 8 are grouped into class I. HDACs 4, 5, 7, and 9 are grouped as class IIA. HDACs 6 and 10 belong to class IIB, while HDAC 11 individually occupies group IV.

HDAC6 is unique among other Zn^{2+}-dependent HDACs. While some HDACs reside in the nucleus and regulate gene transcription, HDAC6 is predominantly found in the cytoplasm and directly engages with a host of cytosolic proteins and substrates, including α-tubulin and β-tubulin, assembled microtubules, cortactin, and heat shock proteins.[9–11] In addition, while histones are the primary substrates for most Zn^{2+}-dependent HDACs, this is not the case for HDAC6 as α-tubulin is proposed to be the major substrate for HDAC6.[12–14] Notably, HDAC6 is structurally distinct from other HDACs, with two unique and independent catalytic domains (CDs) which have diverse roles, and different substrate preference and activity.[15,16] Catalytic domain 2 (CD2) is established as the tubulin deacetylase[17] and a critical target for drug design. HDAC6 also contains a Zn^{2+}-finger ubiquitin binding domain through which it binds to polyubiquitinated proteins and shuttles them to dynein motors associated with microtubule cargo transport.[16] From a therapeutic perspective, several knockout studies in mice lacking the HDAC6 gene have shown no survival dependency and that no lethality is associated with HDAC6 deletion.[18,19]

Currently, the US FDA has approved several HDAC inhibitors for clinical treatment of different hematological cancers including cutaneous T-cell lymphoma (CTCL), peripheral T-cell lymphoma (PTCL), and multiple myeloma (MM). **Vorinostat** (SAHA), was the first FDA-approved HDAC inhibitor in 2006 for CTCL patients whose disease had persisted or worsened after two systemic therapies. As a result of severe side effects, all clinical HDAC inhibitors are approved only for cases where the patient does not respond to first option treatment, or at least two prior standard therapies (**Romidepsin**, approved in 2009 for CTCL patients and in 2011 for PTCL patients, both only after at least one prior systemic therapy; **Panobinostat**, approved in 2016 for multiple myeloma patients after two treatment regimens), or in cases of relapse or recurring disease (**Belinostat**, approved in 2014 for relapsed PTCL). These inhibitors all exhibit pan-HDAC inhibition which may contribute to their side effects.

Since no lethal effects have been observed in HDAC6 knock-out mice, it was hypothesized that selective inhibition may attenuate the toxicity of current clinical HDAC inhibitors while retaining therapeutic efficacy. HDAC6 has been validated as an attractive therapeutic target with modestly selective inhibitors such as **Citarinostat** and **Ricolinostat** currently at different phases of clinical trials, as single agents or combination therapies for several conditions, including refractory multiple myeloma, malignant melanoma, non-small cell lung cancer, lymphoid malignancies, metastatic breast cancer, and diabetic neuropathic pain.[20] These inhibitors achieve selective HDAC6 inhibition by incorporating large bulky cap groups to a lysine hydroxamate mimic, similar to the first non-selective/pan HDAC inhibitor, SAHA (Fig. 1) This scaffold is well tolerated at the outer surface of the HDAC6 binding pocket, unlike other HDAC homologs which are unable to favorably accommodate the cap groups due to steric clashes with the outer surfaces of the binding pockets.[21] The selectivity afforded by these designs does not always translate to a safe therapeutic index and some exhibit moderate to advanced toxicities at clinically efficacious doses.[22–24]

The lead compound described in this study, **TO-317**, exhibits low nanomolar affinity for HDAC6 (K_i = 0.7 nM), low nanomolar inhibition of HDAC6 function (IC_{50} = 2 nM), and over 150-fold selectivity for HDAC6 across a panel of 11 Zn^{2+}-dependent HDACs. The *in vitro* selectivity of **TO-317** for HDAC6 is translated *in cellulo* by Western blot analyses of both pan-HDAC and HDAC6-selective pharmacodynamic (PD) targets. Most interestingly, the X-ray crystal structure determination of **TO-317** bound to HDAC6 CD2 from *Danio rerio* (zebrafish, a well-studied surrogate of human HDAC6 CD2, and henceforth designated *dr*HDAC6) reveals a unique binding mode in which the inhibitor simultaneously coordinates to the catalytic Zn^{2+} ion and participates in a “second shell” interaction with Zn^{2+} by forming a direct hydrogen bond with metal-coordinating residue, H614. A direct enzyme-inhibitor hydrogen bond with this residue has not been previously observed. Exploitation of this structural finding may lead to a new generation of HDAC6-targeting ligands.

Results

Discovery of TO-317, A Potent and Highly Selective HDAC6 Inhibitor:

Herein, we describe a rational, iterative approach to identifying potent and selective HDAC6 inhibitors with drug-like properties and acceptable PK profiles. Identification of novel

inhibitors lacking the high molecular weight cap groups, which contribute to reduced ligand efficiency (LE) and increased molecular weight while not affording selectivity, was considered critical.[25] Examining the binding pocket of HDAC6 revealed a hydrophobic tunnel which opens to an outer cleft region flanked by two outer regions (L1 and L2, Fig. S1B) and an uneven surface topology consisting of polar residues.[26,27] This outer surface region is more expansive in HDAC6 (the rough dimensions of the tunnel entrance are 5.6 Å × 10.8 Å; PDB 5WGI, Fig. S1C) compared to other homologs: the rough dimensions of the tunnel entrance in HDAC3 are 5.6 Å × 5.5 Å (PDB 4A69) and in HDAC8 are 4.9 Å × 6.4 Å (PDB: 1T64) (Fig. S1C). As a result, HDAC6 appears to tolerate inhibitors bearing sterically bulky cap groups, and affords selectivity, as was found for Ricolinostat and Citarinostat.[28] However, bulky cap groups are predominantly solvent exposed with minimal residue interactions, thereby reducing their contributions to HDAC6 binding. From internal hit-to-lead HDACi development and lead optimization,[29,30] compound **1** (Fig 1B, Table 1) was identified, which exhibited low micromolar activity against HDAC6 *in vitro*. Compound **1**, while limited by poor HDAC6 selectivity, poor cellular potency, and an undesirable pharmacokinetic profile, afforded a suitable starting point for optimization due to the presence of a free sulfonamide -NH. Virtual docking of *N*-alkylated derivatives was hypothesized to afford improved binding compounds with better HDAC6-selectivity. Initial docking studies with **1** suggested that F583 and F643 in *dr*HDAC6 CD2 (PDB 5WGI, corresponding to residues F620 and F680 in *Homo sapiens* (human) HDAC6, henceforth designated *h*HDAC6, PDB 5EDU), which line the hydrophobic HDAC6 binding tunnel, form an offset aromatic π-π stacking interaction with the benzyl linker of compound **1**(Fig. S1A). Maintaining this hydrophobic interaction required retention of the benzyl linker group. Linking groups in HDAC6 inhibitors usually direct the cap groups toward the L1 crevice, found in the exposed surface of the enzyme, to facilitate interactions with nearby residues.[26,28,31] With the exception of a small subset of compounds, all reported HDAC6 inhibitors engage only at the L1 region, and in some rare cases, can alternate the positioning of the cap groups between the L1 and L2 crevices.[26,31] (Fig. S1B) The pentafluorobenzene (PFB) ring of **1** was shown to be directed into the L2 region of HDAC6 and is nested on the outer surface with the ring partially exposed to water (Fig. S1A). The PFB ring is predicted to make a π–π aromatic interaction with F643. The sulfonamide -NH does not participate in binding to the protein, despite the predicted interaction with S531, a residue which has previously been proposed to afford selectivity.[32] *N*-Alkylation was therefore not expected to have any disruptive consequences for HDAC6 binding. Water-mediated hydrogen bonding of the sulfonyl oxygen with L712 and the Zn^{2+}-binding ligand, H614, completed the interactions observed with **1** and *dr*HDAC. Structural insights into the binding pockets and the outer surface crevices of HDAC6 (*dr*HDAC6 CD2, PDB: 5WGI) identified several aromatic residues lining the L1 outer surfaces (F642, F643, F583, H463, H573, H614, and Y745) and HDAC6 binding pocket. *N*-alkylation of **1** with a benzyl substituent was proposed to improve binding by these hydrophobic residues via a windmill-type conformation (Fig. S2). Compound **2** was synthesized (Table 1, Fig. S2) and assessed for its inhibitory activity against 4 representative HDAC homologs. HDACi **2** exhibited an improved selectivity window as compared to **1** and both Citarinostat and Ricolinostat. Next, scaffold optimization was attempted by differential substitution of the benzene ring of **2**. Compounds **4** (-CF_3) and **5** (-$N(CH_3)_2$) provided insights into the electronic effects on

activity and selectivity, while **6** (-CH_3) and **7** (-^{t}Bu) elucidated the role of incorporating bulk at the *para*-position. To investigate electron deficient rings, compound **8**, containing a pyridine ring, was synthesized, and was suggested to be the most promising HDAC6 selective inhibitor (>**71 fold**).

Tetrafluorobenzene (TFB) was previously identified as a bio-isostere of PFB, improving phase II metabolic stability, and contributing to improved selectivity for HDAC6.[25,33] PFB was replaced on **8**, **2**, and **3** with a TFB to yield **9**, **10**, and **11**, respectively (Table 2). The location of the fluorine substituent was varied to both the *ortho*- (**13**) and *meta*- (**12**) positions. Potency was marginally improved (2-fold) in both cases, although selectivity was lost. Subsequently, modifications to the pyridine analog were explored. The 2-picolyl substituted inhibitor (**14**) is 2-fold more potent against HDAC6, with only minimal improvement in selectivity when compared to **9**. The 3-picolyl analog, **TO-317** (**15**), showed significant improvements in both potency and selectivity.

In addition to the inhibitory activity in an EMSA assay, binding was measured by an orthogonal fluorescence polarization (FP) assay (Fig. S3), which confirmed an interaction with 4 nM potency between **TO-317** and *dr*HDAC6 CD2. This interaction was substantially tighter when compared to other compounds in the SAR (>20-fold stronger compared to the nearest analog, **11**). Based on the promising activity and binding data, the broader HDAC selectivity of **TO-317** against a panel of all 11 Zn^{2+}-based HDACs was investigated (Fig. 2). **TO-317** was determined to be selective for HDAC6 across all 11 HDAC homologs, showing relatively modest affinity for HDACs 3, 8, and 10 as compared to HDAC6. To further characterize HDAC6 selectivity, **TO-317** was evaluated against the other HDAC homologs at a top treatment concentration of 10 μM. The results, shown in Table 3, support the hypothesis that **TO-317** is a highly selective HDAC6 inhibitor. Further investigation of the selectivity of **TO-317** and its utility as a lead candidate was pursued in a series of structural and cellular biology experiments outlined below.

HDAC6 selectivity mediated by unique catalytic domain interactions:

Computational modelling was employed to investigate the conformation of **TO-317** that afforded HDAC6 selectivity. For comparison, Citarinostat and **TO-317** were docked with *dr*HDAC6 (**PDB 5WGI**, Fig. 3 and Fig. S4-A, respectively). Docking Citarinostat showed the cap group to be largely solvent-exposed and directed away from the L1 and L2 outer surface. The crystal structure of Ricolinostat with the CD2 of *dr*HDAC6 (**PDB 5WGL**) was obtained and an overlay of our docking image of Citarinostat was performed (Fig. S4-A). Both inhibitors adopt identical conformations with the tricyclic pyrimidine cap groups extending away from the L1 crevice without making any apparent interaction with nearby residues, validating the docking results. The authors indicated that water-mediated hydrogen bonding is possible with S531 and D460 residues of the L1 crevice.[28] In contrast, **TO-317** was found to adopt a ligand-enzyme fit that showed scaffold engagement with both L1 & L2 outer crevices (**PDB 5WGI**, Fig. 3). Furthermore, **TO-317** was predicted to adopt a conformation that engaged several residues through aromatic **π-π** interactions and hydrogen bonding. The benzyl linker retained the **π-π** interaction with F643 and F583 observed with compound **1**. The pyridyl ring was predicted to occupy the L2 crevice and engage in a **π-π**

stacking interaction with F642 and H-bonding with the protonated Zn^{2+}-bound, H614. These *in silico* HDAC6 enzyme engagements are absent in comparative HDAC8 studies (**PDB 1T64,** Fig. S4-B, Table S1).

To validate these docking predictions, the X-ray crystal structure of the HDAC6–**TO-317** complex was solved at 1.84 Å resolution (Fig. 4). There are 2 monomers in the asymmetric unit in this orthorhombic crystal form, and the structures of each are essentially identical (root-mean-square deviation = 0.07 Å for 296 Cα atoms). Similarly, the inhibitor binding mode is essentially identical in both monomers, with the hydroxamate moiety coordinating to the catalytic Zn^{2+} ion in a monodentate fashion as first observed for the binding of *N*-hydroxy-4-(2-[(2-hydroxyethyl)(phenyl)amino]-2-oxoethyl)benzamide (HPOB).[15,34] The hydroxamate N-O^- group coordinates to Zn^{2+} with an average separation of 2.4 Å and is hydrogen bonded with Y745. The hydroxamate C=O hydrogen bonds with the Zn^{2+}-bound water molecule, which further engages H573 and H574 in hydrogen bonding.

Outside the active site cleft, the benzyl group of the phenylhydroxamate moiety packs between F583 and F643 and engages in favorable offset π-π interactions. Desolvation of this region may contribute an entropic advantage to the binding of inhibitors with aromatic linker groups.[35] The capping group is bifurcated via the dialkyl sulfonamide nitrogen, with each substituent directed to different pockets in the enzymes binding pocket outer surface. Bifurcated capping groups enable the capture of additional affinity and selectivity interactions in the HDAC6 active site.[32] Notably, the pyridine ring binds in the L1 pocket and accepts a hydrogen bond from Zn^{2+} ligand H614. While water-mediated enzyme-inhibitor hydrogen bonds with H614 have been observed,[28] a direct enzyme-inhibitor hydrogen bond with this residue has not been previously observed. As such, the inhibitor pyridine group serves as a “second shell” or indirect ligand to the catalytic Zn^{2+} ion,[36,37] and chelation of the Zn^{2+} ion by direct and indirect interactions through the hydroxamate group and the pyridine ring, respectively, presumably makes a substantial contribution to .affinity. The sulfonamide group does not participate in any hydrogen bond interactions and is oriented such that the TFB ring is directed towards solution. The closest residue to the TFB ring is S531, which at its closest point is 3.4 Å away.

The molecular residency of **TO-317** at the HDAC6 active site was investigated by kinetic experiments and mass spectrometry analysis. In a jump dilution experiment, **TO-317** exhibited a Ki of 0.7 nM and a residence time of 142 min in a two-step reversible inhibition model (Fig. S5A). This occupancy at the catalytic pocket could rationalize the IC_{50} values exhibited by **TO-317** in enzyme pre-incubation studies (No pre-incubation IC_{50} = 4 nM, 3-hr pre-incubation IC_{50} = 2 nM; IC_{50}’s an average of duplicate studies, Fig. S5B) as intact mass spectrometry analysis confirmed that no covalent modification of the enzyme was observed on treatment with **TO-317** (Fig. S5C). These experiments suggest a reversible, yet thermodynamically driven interaction between **TO-317** and HDAC6 whose stability is presumably driven by the observed dual Zn^{2+}-coordination at the active tunnel.

TO-317 exhibits *in cellulo* HDAC6 target engagement and mediates mechanistic cell proliferation in leukemic cancers:

The cellular potency of **TO-317** was evaluated in a selection of indications where HDAC6 activity has been implicated and treated with HDAC6 inhibitors as single agents. Although HDAC6 has been validated as a clinical target in hematological cancers such as MM, HDAC6 knockout/deletion studies with siRNA or CRISPR/CAS9 show discrepancies in dependency. **TO-317** was assessed across five disease indications (12 cancer cell lines) previously validated by several research groups for their dependency on HDAC6 in growth and survival.[1,38–44] Assessment in acute myeloid leukemia (AML) cell lines was prioritized owing to growing evidence of HDAC6 playing a critical role in survival and resistance to various treatment regimens.[1,42] As can be seen in Fig. 5., **TO-317** was active in several cancer cell lines but showed minimal activity in 'normal' MRC9 lung fibroblasts. **TO-317** was shown to have anti-proliferative activity in all six leukemic cancer cells tested, having an average IC_{50} of <2.0 μM. Sub-μM anti-proliferative activity was observed in both MM cell lines where HDAC6 inhibitors have been deployed clinically.[2,38,40,45]

Acetylation levels of α-tubulin are used as a clinical biomarker for HDAC6 inhibition.[46,47] Inhibition of other HDACs leads to an increase in histone H3K9 and H3K27 acetylation.[48,49] Comparative acetylation of both substrates provides a robust biomarker of HDAC6 inhibition. Treatment of MV4–11 cells with **TO-317** induced a significant increase in Ac-α-tubulin levels, even at 0.25 μM, with only minimal accumulation of Ac-histones (Fig. 6A). From comparative Western blots in **TO-317** and Citarinostat treated MV4–11 cells (0.25 −1.0 μM), it was determined that **TO-317** is marginally more potent for HDAC6 (Fig. 6A) with strong increases in Ac-α-tubulin at concentrations of 0.25 μM. Citarinostat appears more selective than **TO-317** in a cellular environment, with accumulation of Ac-Histone H3K27 between 0.75 −1.00 μM in both AML and MM cells. Similar results were observed in multiple myeloma cell lines (MM.1S cell lines, Fig. 6B) where **TO-317** was more potent for HDAC6 over the range of concentrations assayed. These results recapitulate the selectivity and potency of **TO-317** for HDAC6 *in cellulo*. However, at higher concentrations the effects and cytotoxicity observed may be partially due to nuclear HDAC inhibition.

Immunofluorescence was employed as a secondary biorthogonal assay to validate the *in cellulo* HDAC6 selectivity of **TO-317**. HeLa cells were incubated with two different concentrations of **TO-317** or Citarinostat at 0.1 μM and 2 μM. Treatment with **TO-317** led to significant accumulation of Ac-α-tubulin (red stain) at 2 μM. These effects were slightly less prominent with Citarinostat at the same concentration (Fig. 7 & Fig. S7). The levels of Ac-histone (green stain) do not change significantly upon treatment with either 0.1 μM or 2 μM concentration of **TO-317** (Fig. 7). A DAPI (4′,6-diamidino-2-phenylindole) nuclear stain (blue, Fig. S6) confirmed cell viability during the 6 h incubation period assessed. An overlay of both acetylated tubulin and histone stains also showed preferential Ac-α-tubulin accumulation over Ac-H3K27 histones at all concentrations of **TO-317** (Fig. S6). In conjunction with initial Western blots, immunofluorescence further recapitulated the *in cellulo* HDAC6 target engagement exhibited by **TO-317**.

To characterize the mechanism of inhibition and cell death by **TO-317**, fluorescence activated cell sorting (FACS) flow cytometry was employed to sort the populations of treated leukemic cells at different stages of the cell cycle via their differential staining with annexin and PI fluorophore. Cells in the sub-population UL (upper level, red stain) are necrotic cells and an increase in cell population in this quadrant is indicative of a toxic inhibitor lacking a defined mechanism. **TO-317** does not show statistically different changes to necrosis as this sub-population is consistent across the range of inhibitor concentration tested and comparable to the DMSO control (Fig. 8). The LL sub-population (lower level, green stain) shows viable cells where the fluorophore cannot access the cytosol (green stain) and is representative of intact and healthy cancer cells. The healthy cell count dramatically declines from 88% with no inhibitor present to 35% at 2 μM inhibitor concentration. The loss in healthy cells is compensated in the LR and UR quadrants (blue stains) showing cell populations undergoing early and late apoptosis, respectively. These quadrants show an increase in respective populations as the concentration of **TO-317** is increased. Early and late apoptotic cell populations increased from a combined 11% at 0.25 μM to 65% at 2 μM, and to 73% at 4 μM (Fig. S8-A). A similar trend was observed for Citarinostat (Fig 8, **Panel B;** Fig S8-B), albeit with reduced potency as was seen with **TO-317**. This systematic disruption and arrest of cell cycle is the signature of a mechanistic-based inhibitors, and strongly supports the hypothesis that **TO-317** achieves cell death in leukemia cells through programmed cell death.

The role of reactive oxygen species (ROS) in the progression and survival of leukemic cells has been very contentious.[50] NADPH oxidases (NOX) are elevated in several AML mutations including FLT3-ITD AML and Ras.[51] These mutations are known to be associated with poor prognosis and a high resistance and relapse rates whose mechanism depends on over-secretion of ROS. Several models of AML also show increased ROS generation-induced redox dysregulation and oxidative stress that is strongly linked to promotion of cellular proliferation, survival, and immune evasion.[52] However, several studies also indicate that the persistence of elevated ROS levels may significantly strengthen oxidative DNA damage leading to single and double strand breaks and lipid peroxidation, which further leads to cellular damage. Since HDAC inhibitors are known to generate ROS and induce cell cycle arrest in cancer cells,[53–55] **TO-317** treated MV4–11 cells were investigated. As expected, **TO-317**-treated cells showed increased ROS generation when compared to the DMSO control over a 4 h period (Fig. 9). This is consistent with previously reported HDAC inhibitors and may implicate ROS accumulation as a possible mechanism for the induction of apoptosis observed with **TO-317**.

TO-317 *in vitro* & *in vivo* stability profiles:

Pharmacokinetic profiles of **TO-317** were assessed in both *in vitro* and *in vivo* experiments. Plasma and whole blood stability assays were used to determine the stability of **TO-317** in biological fluids. Several studies have shown reduction of hydroxamic acids in whole blood, but not in plasma.[56,57] After 1 h incubation in mouse plasma, 68% of **TO-317** remained with a calculated $t_{1/2}$ of 110 min (Table. 4). In pooled human whole blood samples, ~69% of **TO-317** was present after 1 h with a calculated $t_{1/2}$ of 108 min, indicating collectively, that **TO-317** does not suffer from the previously reported high clearance rates and metabolic

degradation of *N*-hydroxamic acids in biological fluids.[58,59] **TO-317** was advanced for preclinical pharmacokinetic study employing a dose of 50 mg/kg via intraperitoneal (*i.p.*) injection in male MALB/c mouse. Consistent with previous plasma and whole blood studies, **TO-317** displayed modest stability *in vivo* ($t_{1/2}$ = 1.7 h) as compared to known HDAC inhibitors, reaching a C_{max} of 95.1 ng/mL in 1 h (Fig. 10). However, given the dose, 50 mg/kg, significantly higher plasma concentrations were anticipated, indicating either a metabolic instability *in vivo*, or poor solubility / permeability, which limits systemic bioavailability and further progression as a therapeutic agent.

Kinetic solubility experiments (Fig. S9) showed **TO-317** to exhibit solubility in PBS, pH 7.4 with a saturation concentration of 161.50 ± 33.20 μM (n = 3), ruling out solubility as a likely cause for its poor *in vivo* exposure. PAMPA studies (Table S2) revealed poor permeability profiles which may be responsible for the limited availability observed *in vivo* with **TO-317**, with an average permeability score of $-\log P_e$ = 6.71. Membrane permeable molecules generally exhibit permeability scores with $-\log P_e \leq 6.0$. It is interesting that **TO-317** can elicit PD in proliferating cells such as AML and MM but is unable to passively diffuse in the *i.p.* dosed preclinical experiments.

Future studies will therefore be directed towards improving the permeability properties of **TO-317** *in vivo*, while retaining HDAC6 potency, selectivity, and biological activity.

Discussion

The push for selective HDAC6 inhibitors has been on the rise due to the promising clinical efficacy and lower toxicity profile exhibited in trial. For example, Citarinostat (ACY-241, in combination with lenadomide) is currently in clinical trials for smoldering multiple myeloma; Ricolinostat (ACY-1215) is enrolled in multiple clinical trials for a variety of conditions such as breast cancer, multiple myeloma, diabetic neuropathic pain amongst others.[20,39,43,60] Recent clinical candidates have selectivity windows that are 5–6-fold for HDAC6 as compared to off-target HDACs. While it has been previously reported that HDAC6 has conformational predilections that discriminate between different structural motifs and imposes requirements for inhibitors to achieve maximum ligand-enzyme fit and interactions,[26,31] the clinical HDAC6 inhibitors have instead opted for bulky cap groups to confer selectivity. In this study, by X-ray crystallography, we have shown that **TO-317**, employing a bifurcated approach, using a pyridyl cap group in concert with the traditional N-hydroxamic acid occupies the L1 outer crevice and makes a strong direct H-bonding with the Zn^{2+}-ligand, H614. To the best of our knowledge, there has been no previous report of a direct H-bonding interaction with a Zn^{2+}-ligand at the HDAC6 active site. **TO-317** is shown to adopt an induced fit model which may facilitate this direct residue interaction and thereby stabilize the enzyme-inhibitor complex. This unique structural motif, which engages the second shell interactions with the catalytic Zn^{2+} metal can provide novel pharmacophores for identifying tighter binding HDAC6-selective inhibitors.

The selectivity of **TO-317** was demonstrated *in vitro* through several orthogonal cell biology experiments. We showed in a dose-dependent manner the preferential increase in acetylated α-tubulin on incubation with concentrations as low as 50 nM of **TO-317**. Furthermore,

~0.75 μM was required to observe distinct acetylation of H3 histone, validating the *in vitro* preferential HDAC6 selectivity of **TO-317**. **TO-317** was found to be biologically active in several cancer cell lines, while not eliciting any meaningful cell-killing activity in normal cells, indicating an appreciable therapeutic window, which was attributed to the observed HDAC6 selectivity. **TO-317** mediates programmed cancer cell apoptosis, which may be associated with ROS generation along the mechanistic pathway. Preliminary stability assays in various biological fluids highlighted potential bioavailability issues *in vivo* with this inhibitor. Future studies will attempt to improve the poor bioavailability exhibited by **TO-317**.

Collectively, we have demonstrated a novel approach to selective HDAC6 inhibition, achieving low nM potency against HDAC6. Structural studies have revealed a unique binding mode in which **TO-317** simultaneously coordinates to Zn^{2+} and the H614 residue in the catalytic tunnel, affording >150-fold selectivity for HDAC6. Optimized PK properties might yield a preclinical candidate HDAC6 inhibitor from this compound. Finally, the **TO-317** model presents a structural model that can be incorporated for the selective targeting of HDAC6.

Experimental Section

Chemistry:

All chemicals and reagents were purchased from any of the following suppliers – Combi-Blocks, Sigma-Aldrich, Enamine, Alfa-Aesar, and Oakwood Chemicals. Solvents such as DCM were obtained in anhydrous forms from our in-house Mbraun solvent dispensary system. Other solvents such as acetonitrile and DMF were used in their dry forms from 100 mL Sigma-Aldrich bottles. Reactions were carried out in oven-dried glassware, and reaction progress monitored using a TLC silica gel 60 F254 and a 254 nM UV lamp. Purification of intermediates were carried out using a Biotage automated flash chromatography instrument, in pre-packed SNAP KP-SIL cartridges supplied by Biotage in sizes of 12G, 25G, 50G, and 100G packings. Characterization for intermediates include ^{1}H, ^{19}F, and ^{13}C NMR obtained using a 400 MHz Bruker NMR spectrometer, low-res mass spectrometry obtained using a Waters LC-MS Micromass ZQ using ESI positive and negative ionization modes. Purifications of final compounds were carried out using a Waters prep-HPLC system equipped with Waters 2545 quaternary gradient pump system, XSelect 300G CSH Phenyl-Hexyl C18 column, 2489 dual absorbance UV detector, and ran using mobile phases acetonitrile and water spiked with 0.1% TFA. Characterization for final compounds include ^{1}H, ^{19}F, and ^{13}C NMR and are obtained like the intermediates, high-res mass spectrometry collected using a quadrupole time of flight LC/MS system at the Advanced Instrumentation for Molecular Structure (AIMS) facility at the University of Toronto, purity check for all final compounds satisfy a ≥95% purity requirement and traces were collected using a HP 1100 series analytical HPLC using gradient 5% - 100% Acetonitrile in water for 40 mins / 60 mins. The retention times (T_R) and purity as calculated from peak area of compound / total area of all peaks in spectra X 100% were reported as automatically calculated by the analytical HPLC instrument.

Details for protein crystallographic methods are provided in detail in the online supplementary information.

All intermediates and final product characterizations and their yields are reported in the online supplementary information.

Synthesis of Product A' (Tetrafluorobenzenesulfonyl Chloride):

Tetrafluorobenzene (1.0 g, 6.6 mmol) was carefully added into chlorosulfonic acid (3.88 g, 33.3 mmol) and the mixture was refluxed for 3 hrs. Reaction vessel was cooled to 0 °C, and the solution was slowly pipetted into ice-cold water. This aqueous solution was extracted with 20 mL EtOAc twice. Combined EtOAc fractions were washed with brine and dried over $MgSO_4$. Clear solution was concentrated under vacuum and purified using flash chromatography, isocratic condition 10% EtOAc in Hexane. Pure product was collected as a clear oil, 95% yield. ^{1}H NMR (400 MHz, Acetonitrile-d_3) δ 7.92 – 7.66 (m, 1H).,^{19}F NMR (376 MHz, Acetonitrile-d_3) δ −133.82 (dtd, J = 20.7, 12.0, 5.9 Hz), −135.65 – −136.10 (m), −142.87 (tdd, J = 19.2, 12.0, 7.8 Hz), −151.06 – −151.57 (m). ^{13}C NMR (101 MHz, Acetonitrile-d_3) δ 147.8 (ddd, J = 10.7, 3.8, 1.8 Hz), 147.3 (ddd, J = 15.8, 12.3, 3.1 Hz), 146.7 (dt, J = 12.7, 3.3 Hz), 145.3 (ddd, J = 10.8, 3.9, 1.8 Hz), 144.6 (ddd, J = 15.9, 12.3, 3.1 Hz), 144.1 (dt, J = 12.7, 3.3 Hz), 143.1 (ddd, J = 16.0, 13.0, 3.2 Hz), 140.5 (ddd, J = 16.1, 12.9, 3.2 Hz), 127.4 (ddd, J = 11.6, 6.8, 4.4 Hz), 116.6, 111.8 (dd, J = 23.4, 3.5 Hz). MS ESI- Found 229.04 corresponding to M-1 for the acid showing rapid compound hydrolysis under MS conditions. Also found 459.0 (M+M+1 peak)

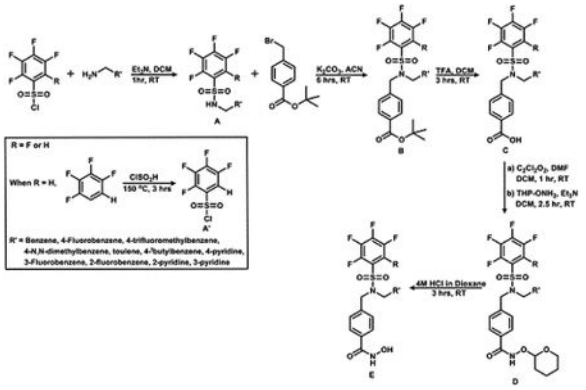

Synthesis of Product A (Secondary Sulfonamides):

In an oved-dried round bottom flask charged with a magnetic stirring bar was added 1 molar equivalence of the corresponding sulfonyl chloride and 1.1 molar equivalent of the corresponding amine in 0.1M DCM solution and the mixture is stirred at RT under inert conditions for 1 hr or until TLC confirms complete consumption of starting materials. An insoluble precipitate is usually formed corresponding to the protonated quaternary sulfonamide product which is neutralized on addition of 2 molar equivalence of the triethylamine base usually leading to dissolution of the precipitate and a clear solution. This clear solution is further stirred for an additional 10 minutes. Reaction solvents are removed under vacuum and residue obtained is dissolved in 2:1 mixture of EtOAc : H_2O. The organic

layer is washed with brine and dried over $MgSO_4$. The organic solution is evaporated and purified by flash chromatography using conditions as determined by TLC.

Synthesis of Product B (Tertiary Sulfonamide, Ester Derivatives):

To the corresponding secondary sulfonamides (1 eq.) was added under inert conditions 1.1 molar equivalent of tert-butyl 4-(bromomethyl) benzoate and K_2CO_3 (2 eq.) in 0.25M acetonitrile solution. Mixture was stirred for 6 hours at room temperature, then the acetonitrile solvent is removed, and the solid residue obtained is dissolved in EtOAc and washed with H_2O. Organic layer is further washed with brine and dried over $MgSO_4$. The clear solution obtained is concentrated and purified using flash chromatography at the appropriate conditions as determined by TLC.

Synthesis of Product C: (Tertiary Sulfonamides, Acid Derivatives):

The corresponding ester is dissolved in 1:4 TFA : DCM (0.1M solution) and stirred for 3 hrs or until TLC indicates complete deprotection of the ester. Acidic solution is then neutralized with sodium bicarbonate to a pH of ~8 before extracting 3x using appropriate amounts of DCM. The combined organic phase is washed once with brine and dried over $MgSO_4$. Clear organic solution is evaporated under vacuum to give the required acid which is carried forward to the next step without any further purification.

Synthesis of Compound D: O-(Tetrahydro-2H-pyran-2-yl) Protected Hyrodoxamate Esters:

In an oven-dried round bottom flask was added the corresponding acid dissolved in 0.2M DCM containing few drops of DMF. This solution is cooled to 0 °C, and 5 molar equivalent oxalic chloride is added resulting in wild evolution of CO_2 gas. On complete effervescence, the solution is warmed to room temperature and then allowed to stir for 1 hr. After stirring for 1 hr, the solvents areremoved by evaporation and the residue usually obtained is dried under vacuum for 1 hr. The dried chloride residue is further taken up in 0.5M DCM and 1.5 molar equivalent of O-(Tetrahydro-2H-pyran-2-yl)hydroxylamine resulting in a cloudy mixture which is stirred for 15 minutes before the addition of 2 molar equivalent triethylamine which results in a clear solution. This mixture is further stirred for 1 hr or as judged to be completion of reaction by TLC. The DCM solvent is then removed under vacuum, dissolved in H_2O and extracted with EtOAc. The organic layer is washed with brine then dried over $MgSO_4$ before being purified using flash chromatography based on conditions as determined by TLC.

Synthesis of Final Compounds: Corresponding Hydroxamic Acids:

The precursor hydroxamate ester is dissolved in 0.1M solution of 4M HCl in Dioxane and the acidic solution was stirred for 3 hrs. or until TLC indicates complete consumption of the starting material. The acid solution is removed under vacuum and the crude hydroxamic acid is taken up in 2 – 5 mL mixture of H_2O: Acetonitrile in proportions that is suitable for dissolution. A 200 mL aliquot is subjected to an analytical HPLC trial run (5% - 100% acetonitrile in H_2O) to determine appropriate conditions for preparatory HPLC purification runs. About 2 – 5 mL of reaction mixture is then subjected to a preparatory HPLC run, 5% - 95% acetonitrile or gradient conditions as determined from analytical HPLC trial run.

Fractions from prep-HPLC are further checked by analytical HPLC for purity check, and then analyzed by LCMS for identity check before pure fractions are pooled together and lyophilized overnight to give the pure dry hydroxamic acids.

Cytotoxicity assays: HeLa cells were grown in Dulbecco's Modified Eagles Medium (DMEM) supplemented with 10% Fetal Bovine Serum (FBS) (Sigma-Aldrich). MV4–11 and AML3 were maintained in Iscove's Modified Dulbecco's Medium (IMDM) supplemented with 10% FBS. MOLM-13, MRC-9, MM.1S, MM.1R, Jukat, BV-173 and RPMI 8226 cells were maintained in RPMI-1640 and supplemented with 10% FBS. U87G cells were maintained in Eagle's Minimum Essential Medium (EMEM) and supplemented with 10% FBS.AR230 cells were maintained in RPMI-1640 and supplemented with 10% FBS, 2 mM L-Glutamine and 1 μM Imatinib. Normal Human Fibroblasts (NHF) were purchased from Cell System and grown in Cell System growth medium, supplemented with Culture Boost. HUVEC cells were purchased from ATCC and cultured in Vascular Cell Basal medium supplemented with Endothelial Cell Grow Kit-VEGF. Appropriate number of cells were plated per well in 96-well flat-bottom sterile culture plates with low-evaporation lids (Costar #3997) for these cell lines. After 24 h, inhibitors and a vehicle control (0.5% DMSO) were added. Wells were treated with Cell Titer-Blue® (Promega #G808A) (20 μL/well) after 72 h and fluorescence was recorded at 560/590 nm using a Cytation S63 spectrophotometer. IC_{50} values were determined using non-linear regression analysis with GraphPad Prism 6.0 (GraphPad Software Inc.).

FACs Apoptosis Detection Assay: MV4–11 cells were cultured, dosed, and washed twice with cold 1X PBS. Using FITC Annexin V Apoptosis Detection Kit I (BD Pharmingen), cell pellets were resuspended in 1X binding buffer at a density of 1×10^6 cells/ml. 5 μL FITC Annexin V and 5 μL Propidium Iodide (PI) were added to 250 μL of solution (2.5×10^5 cells). Cells were vortexed and incubated in the dark for 15 min, followed by addition of 250 μL of 1X binding buffer. Cells were analyzed by flow cytometry within 1 hour using Cytoflex S (Beckman Coulter).

Western blotting: MV4–11 and MM.1S cells were incubated with compounds for 6 hours, before lysing with radioimmunoprecipitation assay (RIPA) buffer (20 mM Tris pH 7.4, 150 mM NaCl, 0.5% deoxycholate, 1% Triton X-100, and 0.1% sodium dodecyl sulfate (SDS)). Total protein was measured using a BCA assay (ThermoFisher), in which clarified protein was resolved on a 4 – 20% polyacrylamide SDS gel and transferred to a nitrocellulose membrane (Bio-Rad). The membranes were blocked with a 5% solution of skimmed milk powder in PBST, followed by an overnight incubation at 4 °C in primary antibody (1:1000 dilution). Blots were probed with antibodies against acetylated alpha-tubulin mouse monoclonal (EMD Millipore), acetylated histone H3 (Ac-Lys18, Sigma) and HSC70 (Santa Cruz). Horseradish peroxidase (HRP)-conjugated goat anti-mouse IgG secondary antibody (Cell Signaling) or HRP-linked anti-rabbit IgG secondary antibody (Cell Signaling) were applied to the membrane (1:5000 dilution) and bands were visualized using clarity western ECL substrate luminal/enhancer solution and peroxide solution 1:1 ratio for HRP-conjugated secondary antibody (Bio-Rad) and analyzed using Image lab software (Bio-Rad).

Detection of ROS Generation: MV4–11 cells were treated with the relevant compounds and analyzed for production of ROS using DCFDA (Abcam 113851 DCFDA Cellular ROS detection Assay Kit). Briefly, cells were collected and washed with 1× PBS once and incubated with DCFDA (33 μM) at 37 °C for 30 min in the dark. The cells were then washed and resuspended in 1X supplemental buffer, seeded in a clear bottom black 96-well plate (Fisher Scientific), dosed with compound and fluorescence at Ex/Em=485/535 was measured using a Cytation S63 spectrophotometer.

Immunofluorescence Assay: HeLa cells were plated to sub-confluency on a clear bottom black 96-well plate (Fisher Scientific) and treated with compound after 24 h. Samples were washed with 1× PBS, fixed with 4% formaldehyde (Millipore Sigma), permeabilized with 1% Triton X-100 (Millipore Sigma), and blocked in 5% bovine serum albumin (BSA) (BioShop) for 1 hour at room temperature. The cells were incubated in an antibody cocktail made up of acetylated alpha-tubulin mouse monoclonal (1:100 dilution, MD Millipore) and acetylated histone H3 (1:50 dilution, Ac-Lys18, Sigma). Cells were counterstained for nucleic acids using 4′,6-diamidino-2-phenylindole (DAPI) (ThermoFisher Scientific). Images were acquired using a Cytation S63 spectrophotometer.

Further protocols have been provided in supplementary methods

Supplementary Material

Refer to Web version on PubMed Central for supplementary material.

Funding Sources

P.T.G is supported by research grants from NSERC (RGPIN-2014-05767), CIHR (MOP-130424, MOP-137036), Canada Research Chair (950-232042), Canadian Cancer Society (703963), Canadian Breast Cancer Foundation (705456), Leukaemia and Lymphoma Society of Canada and infrastructure grants from CFI (33536) and the Ontario Research Fund (34876). D.W.C. is supported by grant GM49758 from the US National Institutes of Health. O.O.O. is supported by an OGS Fellowship. Y.S.R and N.N are supported by grants from Jesse's Journey and A.D.C is supported by NSERC CGS. This work utilized beamline 17-ID-1 (AMX) of the National Synchroton Light Source II, a US Department of Energy (DOE) Office of Science User Facility operated for the DOE office of Science by Brookhaven National Laboratory under contract DE-SC0012704. The Center for BioMolecular Structure (CBMS) is primarily supported by the National Institute of General Medical Sciences (NIGMS) of the National Institutes of Health through a Center Core P30 Grant (P30GM133893) and by the DOE Office of Biological and Environmental Research (KP1605010). The authors would also like to thank Andrew Sedmihradsky and family, who have raised funds, awareness for DMD and generated support for Max's Big Fellowship.

Abbreviations:

CAS9	CRISPR associated protein 9
CD	catalytic domain
CRISPR	Clustered Regularly Interspaced Short Palindromic Repeats
CTCL	Cutaneous T-Cell Lymphoma
DAPI	4′,6-diamidino-2-phenylindole
***dr*HDAC6**	*danio rerio* Histone Deacetylase 6

EMSA	Electrophoretic Mobility Shift Assay
FP	Fluorescence Polarization
HDAC	Histone Deactylase
HDAC6	Histone Deacetylase 6
LE	Ligand Efficiency
LL	Lower Left
LR	Lower Right
MM	Multiple Myeloma
PFB	Pentafluoro Benzene
PI	Propidium Iodide
PTCL	Peripheral T-Cell Lymphoma
TFB	Tetrafluoro Benzene
UL	Upper Left
UR	Upper Right

References

(1). Hackanson B; Rimmele L; Benkißer M; Abdelkarim M; Fliegauf M; Jung M; Lübbert M HDAC6 as a Target for Antileukemic Drugs in Acute Myeloid Leukemia. Leukemia Research 2012, 36 (8), 1055–1062. 10.1016/j.leukres.2012.02.026. [PubMed: 22464548]

(2). Santo L; Hideshima T; Kung AL; Tseng JC; Tamang D; Yang M; Jarpe M; Van Duzer JH; Mazitschek R; Ogier WC; et al. Preclinical Activity, Pharmacodynamic, and Pharmacokinetic Properties of a Selective HDAC6 Inhibitor, ACY-1215, in Combination with Bortezomib in Multiple Myeloma. Blood 2012, 119 (11), 2579–2589. 10.1182/blood-2011-10-387365. [PubMed: 22262760]

(3). Wang Z; Tang F; Hu P; Wang Y; Gong J; Sun S; Xie C HDAC6 Promotes Cell Proliferation and Confers Resistance to Gefitinib in Lung Adenocarcinoma. Oncology Reports 2016, 36 (1), 589–597. 10.3892/or.2016.4811. [PubMed: 27221381]

(4). Ho TCS; Chan AHY; Ganesan A Thirty Years of HDAC Inhibitors: 2020 Insight and Hindsight. Journal of Medicinal Chemistry 2020, 63 (21), 12460–12484. 10.1021/acs.jmedchem.0c00830. [PubMed: 32608981]

(5). Wang P; Wang Z; Liu J Role of HDACs in Normal and Malignant Hematopoiesis. Molecular Cancer. 2020. 10.1186/s12943-019-1127-7.

(6). Zhao C; Dong H; Xu Q; Zhang Y Histone Deacetylase (HDAC) Inhibitors in Cancer: A Patent Review (2017-Present). Expert Opinion on Therapeutic Patents 2020, 30 (4), 263–274. 10.1080/13543776.2020.1725470. [PubMed: 32008402]

(7). Leipe DD; Landsman D Histone Deacetylases, Acetoin Utilization Proteins and Acetylpolyamine Amidohydrolases Are Members of an Ancient Protein Superfamily. Nucleic Acids Research 1997, 25 (18), 3693–3697. 10.1093/nar/25.18.3693. [PubMed: 9278492]

(8). Gregoretti IV; Lee YM; Goodson HV Molecular Evolution of the Histone Deacetylase Family: Functional Implications of Phylogenetic Analysis. Journal of Molecular Biology 2004, 338 (1), 17–31. 10.1016/j.jmb.2004.02.006. [PubMed: 15050820]

(9). Rossaert E; Van Den Bosch L HDAC6 Inhibitors: Translating Genetic and Molecular Insights into a Therapy for Axonal CMT. Brain Research. 2020. 10.1016/j.brainres.2020.146692.

(10). Auzmendi-Iriarte J; Saenz-Antoñanzas A; Mikelez-Alonso I; Carrasco-Garcia E; Tellaetxe-Abete M; Lawrie CH; Sampron N; Cortajarena AL; Matheu A Characterization of a New Small-Molecule Inhibitor of HDAC6 in Glioblastoma. Cell Death and Disease 2020, 11 (6). 10.1038/s41419-020-2586-x.

(11). Park JK; Jang YJ; Oh BR; Shin J; Bae D; Ha N; Choi Y Il; Youn GS; Park J; Lee EY; et al. Therapeutic Potential of CKD-506, a Novel Selective Histone Deacetylase 6 Inhibitor, in a Murine Model of Rheumatoid Arthritis. Arthritis Research and Therapy 2020, 22 (1). 10.1186/s13075-020-02258-0.

(12). Boyault C; Sadoul K; Pabion M; Khochbin S HDAC6, at the Crossroads between Cytoskeleton and Cell Signaling by Acetylation and Ubiquitination. Oncogene. 2007, pp 5468–5476. 10.1038/sj.onc.1210614. [PubMed: 17694087]

(13). Moreno-Gonzalo O; Mayor F; Sánchez-Madrid F HDAC6 at Crossroads of Infection and Innate Immunity. Trends in Immunology. 2018, pp 591–595. 10.1016/j.it.2018.05.004. [PubMed: 29937401]

(14). Depetter Y; Geurs S; De Vreese R; Goethals S; Vandoorn E; Laevens A; Steenbrugge J; Meyer E; de Tullio P; Bracke M; et al. Selective Pharmacological Inhibitors of HDAC6 Reveal Biochemical Activity but Functional Tolerance in Cancer Models. International Journal of Cancer 2019, 145 (3), 735–747. 10.1002/ijc.32169. [PubMed: 30694564]

(15). Hai Y; Christianson DW Histone Deacetylase 6 Structure and Molecular Basis of Catalysis and Inhibition. Nature Chemical Biology 2016, 12 (9), 741–747. 10.1038/nchembio.2134. [PubMed: 27454933]

(16). Miyake Y; Keusch JJ; Wang L; Saito M; Hess D; Wang X; Melancon BJ; Helquist P; Gut H; Matthias P Structural Insights into HDAC6 Tubulin Deacetylation and Its Selective Inhibition. Nature Chemical Biology 2016, 12 (9), 748–754. 10.1038/nchembio.2140. [PubMed: 27454931]

(17). Haggarty SJ; Koeller KM; Wong JC; Grozinger CM; Schreiber SL Domain-Selective Small-Molecule Inhibitor of Histone Deacetylase 6 (HDAC6)-Mediated Tubulin Deacetylation. Proceedings of the National Academy of Sciences of the United States of America 2003, 100 (8), 4389–4394. 10.1073/pnas.0430973100. [PubMed: 12677000]

(18). Zhang Y; Kwon S; Yamaguchi T; Cubizolles F; Rousseaux S; Kneissel M; Cao C; Li N; Cheng H-L; Chua K; et al. Mice Lacking Histone Deacetylase 6 Have Hyperacetylated Tubulin but Are Viable and Develop Normally. Molecular and Cellular Biology 2008, 28 (5), 1688–1701. 10.1128/mcb.01154-06. [PubMed: 18180281]

(19). Messaoudi K; Ali A; Ishaq R; Palazzo A; Sliwa D; Bluteau O; Souquère S; Muller D; Diop KM; Rameau P; et al. Critical Role of the HDAC6-Cortactin Axis in Human Megakaryocyte Maturation Leading to a Proplatelet-Formation Defect. Nature Communications 2017, 8 (1). 10.1038/s41467-017-01690-2.

(20). Shen S; Kozikowski AP A Patent Review of Histone Deacetylase 6 Inhibitors in Neurodegenerative Diseases (2014–2019). Expert Opinion on Therapeutic Patents. 2020, pp 121–136. 10.1080/13543776.2019.1708901. [PubMed: 31865813]

(21). Mackwitz MKW; Hamacher A; Osko JD; Held J; Schöler A; Christianson DW; Kassack MU; Hansen FK Multicomponent Synthesis and Binding Mode of Imidazo[1,2- a]Pyridine-Capped Selective HDAC6 Inhibitors. Organic Letters 2018, 20 (11), 3255–3258. 10.1021/acs.orglett.8b01118. [PubMed: 29790770]

(22). Chia PL; Mukhopadhyay P; Kelly S; Wu R; Fenn K; Trivedi MS Network-Based Assessment of HDAC6 Activity Is Highly Predictive of Pre-Clinical and Clinical Responses to the HDAC Inhibitor Ricolinostat. medRxiv 2020.

(23). Jochems J; Boulden J; Lee BG; Blendy JA; Jarpe M; Mazitschek R; Van Duzer JH; Jones S; Berton O Antidepressant-like Properties of Novel HDAC6-Selective Inhibitors with Improved Brain Bioavailability. Neuropsychopharmacology 2014, 39 (2), 389–400. 10.1038/npp.2013.207. [PubMed: 23954848]

(24). Vergani B; Sandrone G; Marchini M; Ripamonti C; Cellupica E; Galbiati E; Caprini G; Pavich G; Porro G; Rocchio I; et al. Novel Benzohydroxamate-Based Potent and Selective Histone Deacetylase 6 (HDAC6) Inhibitors Bearing a Pentaheterocyclic Scaffold: Design, Synthesis, and

Biological Evaluation. Journal of Medicinal Chemistry 2019, 62 (23), 10711–10739. 10.1021/acs.jmedchem.9b01194. [PubMed: 31710483]

(25). Shouksmith AE; Shah F; Grimard ML; Gawel JM; Raouf YS; Geletu M; Berger-Becvar A; De Araujo ED; Luchman HA; Heaton WL; et al. Identification and Characterization of AES-135, a Hydroxamic Acid-Based HDAC Inhibitor That Prolongs Survival in an Orthotopic Mouse Model of Pancreatic Cancer. Journal of Medicinal Chemistry 2019, 62 (5), 2651–2665. 10.1021/acs.jmedchem.8b01957. [PubMed: 30776234]

(26). Porter NJ; Osko JD; Diedrich D; Kurz T; Hooker JM; Hansen FK; Christianson DW Histone Deacetylase 6-Selective Inhibitors and the Influence of Capping Groups on Hydroxamate-Zinc Denticity. Journal of Medicinal Chemistry 2018, 61 (17), 8054–8060. 10.1021/acs.jmedchem.8b01013. [PubMed: 30118224]

(27). Shen S; Svoboda M; Zhang G; Cavasin MA; Motlova L; McKinsey TA; Eubanks JH; Bařinka C; Kozikowski AP Structural and in Vivo Characterization of Tubastatin A, a Widely Used Histone Deacetylase 6 Inhibitor. ACS Medicinal Chemistry Letters 2020, 11 (5), 706–712. 10.1021/acsmedchemlett.9b00560. [PubMed: 32435374]

(28). Porter NJ; Mahendran A; Breslow R; Christianson DW Unusual Zinc-Binding Mode of HDAC6-Selective Hydroxamate Inhibitors. Proceedings of the National Academy of Sciences of the United States of America 2017, 114 (51), 13459–13464. 10.1073/pnas.1718823114. [PubMed: 29203661]

(29). Gawel JM; Shouksmith AE; Raouf YS; Nawar N; Toutah K; Bukhari S; Manaswiyoungkul P; Olaoye OO; Israelian J; Radu TB; et al. PTG-0861: A Novel HDAC6-Selective Inhibitor as a Therapeutic Strategy in Acute Myeloid Leukaemia. European Journal of Medicinal Chemistry 2020, 201. 10.1016/j.ejmech.2020.112411.

(30). Shouksmith AE; Gawel JM; Nawar N; Sina D; Raouf YS; Bukhari S; He L; Johns AE; Manaswiyoungkul P; Olaoye OO; et al. Class I/IIb-Selective HDAC Inhibitor Exhibits Oral Bioavailability and Therapeutic Efficacy in Acute Myeloid Leukemia. ACS Medicinal Chemistry Letters 2020, 11 (1), 56–64. 10.1021/acsmedchemlett.9b00471. [PubMed: 31938464]

(31). Osko JD; Christianson DW Structural Basis of Catalysis and Inhibition of HDAC6 CD1, the Enigmatic Catalytic Domain of Histone Deacetylase 6. Biochemistry 2019, 58 (49), 4912–4924. 10.1021/acs.biochem.9b00934. [PubMed: 31755702]

(32). Osko JD; Christianson DW Structural Determinants of Affinity and Selectivity in the Binding of Inhibitors to Histone Deacetylase 6. Bioorganic and Medicinal Chemistry Letters. 2020. 10.1016/j.bmcl.2020.127023.

(33). Ali AM; Gómez-Biagi RF; Rosa DA; Lai PS; Heaton WL; Park JS; Eiring AM; Vellore NA; De Araujo ED; Ball DP; et al. Disarming an Electrophilic Warhead: Retaining Potency in Tyrosine Kinase Inhibitor (TKI)-Resistant CML Lines While Circumventing Pharmacokinetic Liabilities. ChemMedChem 2016, 11 (8), 850–861. 10.1002/cmdc.201600021. [PubMed: 27028877]

(34). Porter NJ; Christianson DW Structure, Mechanism, and Inhibition of the Zinc-Dependent Histone Deacetylases. Current Opinion in Structural Biology. 2019, pp 9–18. 10.1016/j.sbi.2019.01.004.

(35). Porter NJ; Wagner FF; Christianson DW Entropy as a Driver of Selectivity for Inhibitor Binding to Histone Deacetylase 6. Biochemistry 2018, 57 (26), 3916–3924. 10.1021/acs.biochem.8b00367. [PubMed: 29775292]

(36). Christianson DW; Fierke CA Carbonic Anhydrase: Evolution of the Zinc Binding Site by Nature and by Design. Accounts of Chemical Research 1996, 29 (7), 331–339. 10.1021/ar9501232.

(37). Dudev T; Lin Y. lin; Dudev M; Lim C First-Second Shell Interactions in Metal Binding Sites in Proteins: A PDB Survey and DFT/CDM Calculations. Journal of the American Chemical Society 2003, 125 (10), 3168–3180. 10.1021/ja0209722. [PubMed: 12617685]

(38). Ray A; Das DS; Song Y; Hideshima T; Tai YT; Chauhan D; Anderson KC Combination of a Novel HDAC6 Inhibitor ACY-241 and Anti-PD-L1 Antibody Enhances Anti-Tumor Immunity and Cytotoxicity in Multiple Myeloma. Leukemia. 2018, pp 843–846. 10.1038/leu.2017.322. [PubMed: 29104288]

(39). Yee AJ; Bensinger W; Voorhees PM; Berdeja JG; Richardson PG; Supko J; Tamang D; Jones SS; Wheeler C; Markelewicz RJ; et al. Ricolinostat (ACY-1215), the First Selective HDAC6 Inhibitor, in Combonation with Lenalidomide and Dexamethasone in Patients with Relapsed and

Relapsed-and-Refractory Multiple Myeloma: Phase 1b Results (ACE-MM-101 Study). Blood 2015, 126 (23), 3055–3055. 10.1182/blood.v126.23.3055.3055.

(40). Hideshima T; Qi J; Paranal RM; Tang W; Greenberg E; West N; Colling ME; Estiu G; Mazitschek R; Perry JA; et al. Discovery of Selective Small-Molecule HDAC6 Inhibitor for Overcoming Proteasome Inhibitor Resistance in Multiple Myeloma. Proceedings of the National Academy of Sciences of the United States of America 2016, 113 (46), 13162–13167. 10.1073/pnas.1608067113. [PubMed: 27799547]

(41). Wang Z; Hu P; Tang F; Lian H; Chen X; Zhang Y; He X; Liu W; Xie C HDAC6 Promotes Cell Proliferation and Confers Resistance to Temozolomide in Glioblastoma. Cancer Letters 2016, 379 (1), 134–142. 10.1016/j.canlet.2016.06.001. [PubMed: 27267806]

(42). Maharaj K; Powers JJ; Achille A; Deng S; Fonseca R; Pabon-Saldana M; Quayle SN; Jones SS; Villagra A; Sotomayor EM; et al. Silencing of HDAC6 as a Therapeutic Target in Chronic Lymphocytic Leukemia. Blood Advances 2018, 2 (21), 3012–3024. 10.1182/bloodadvances.2018020065. [PubMed: 30425065]

(43). Cosenza M; Civallero M; Quayle SN; Sacchi S; Pozzi S Ricolinostat (ACY-1215), a Selective HDAC6 Inhibitor, Alone and in Combination with Bendamustine Is Effective in Preclinical Studies in Lymphoma Cell Lines. Blood 2016, 128 (22), 2772–2772. 10.1182/blood.v128.22.2772.2772.

(44). Cosenza M; Civallero M; Marcheselli L; Sacchi S; Pozzi S Ricolinostat, a Selective HDAC6 Inhibitor, Shows Anti-Lymphoma Cell Activity Alone and in Combination with Bendamustine. Apoptosis 2017, 22 (6), 827–840. 10.1007/s10495-017-1364-4. [PubMed: 28315173]

(45). Guha M HDAC Inhibitors Still Need a Home Run, despite Recent Approval. Nature Reviews Drug Discovery. 2015, pp 225–226. 10.1038/nrd4583.

(46). Hubbert C; Guardiola A; Shao R; Kawaguchi Y; Ito A; Nixon A; Yoshida M; Wang XF; Yao TP HDAC6 Is a Microtubule-Associated Deacetylase. Nature 2002, 417 (6887), 455–458. 10.1038/417455a. [PubMed: 12024216]

(47). Catley L; Weisberg E; Kiziltepe T; Tai YT; Hideshima T; Neri P; Tassone P; Atadja P; Chauhan D; Munshi NC; et al. Aggresome Induction by Proteasome Inhibitor Bortezomib and α-Tubulin Hyperacetylation by Tubulin Deacetylase (TDAC) Inhibitor LBH589 Are Synergistic in Myeloma Cells. Blood 2006, 108 (10), 3441–3449. 10.1182/blood-2006-04-016055. [PubMed: 16728695]

(48). Sanchez GJ; Richmond PA; Bunker EN; Karman SS; Azofeifa J; Garnett AT; Xu Q; Wheeler GE; Toomey CM; Zhang Q; et al. Genome-Wide Dose-Dependent Inhibition of Histone Deacetylases Studies Reveal Their Roles in Enhancer Remodeling and Suppression of Oncogenic Super-Enhancers. Nucleic Acids Research 2018, 46 (4), 1756–1776. 10.1093/nar/gkx1225. [PubMed: 29240919]

(49). Lue JK; Prabhu SA; Liu Y; Gonzalez Y; Verma A; Mundi PS; Abshiru N; Camarillo JM; Mehta S; Chen EI; et al. Precision Targeting with EZH2 and HDAC Inhibitors in Epigenetically Dysregulated Lymphomas. Clinical Cancer Research 2019, 25 (17), 5271–5283. 10.1158/1078-0432.CCR-18-3989. [PubMed: 30979734]

(50). Yang H; Villani RM; Wang H; Simpson MJ; Roberts MS; Tang M; Liang X The Role of Cellular Reactive Oxygen Species in Cancer Chemotherapy. Journal of Experimental and Clinical Cancer Research. 2018. 10.1186/s13046-018-0909-x.

(51). Jayavelu AK; Müller JP; Bauer R; Böhmer SA; Lässig J; Cerny-Reiterer S; Sperr WR; Valent P; Maurer B; Moriggl R; et al. NOX4-Driven ROS Formation Mediates PTP Inactivation and Cell Transformation in FLT3ITD-Positive AML Cells. Leukemia 2016, 30 (2), 473–483. 10.1038/leu.2015.234. [PubMed: 26308771]

(52). Zhou F; Shen Q; Claret FX Novel Roles of Reactive Oxygen Species in the Pathogenesis of Acute Myeloid Leukemia. Journal of Leukocyte Biology 2013, 94 (3), 423–429. 10.1189/jlb.0113006. [PubMed: 23715741]

(53). Eckschlager T; Plch J; Stiborova M; Hrabeta J Histone Deacetylase Inhibitors as Anticancer Drugs. International Journal of Molecular Sciences. 2017. 10.3390/ijms18071414.

(54). Debeb BG; Lacerda L; Larson R; Wolfe AR; Krishnamurthy S; Reuben JM; Ueno NT; Gilcrease M; Woodward WA Histone Deacetylase Inhibitor-Induced Cancer Stem Cells Exhibit High

Pentose Phosphate Pathway Metabolism. Oncotarget 2016, 7 (19), 28329–28339. 10.18632/oncotarget.8631. [PubMed: 27078845]

(55). Valdez BC; Brammer JE; Li Y; Murray D; Liu Y; Hosing C; Nieto Y; Champlin RE; Andersson BS Romidepsin Targets Multiple Survival Signaling Pathways in Malignant T Cells. Blood Cancer Journal 2015, 5 (10). 10.1038/bcj.2015.83.

(56). Freisleben A; Brudny-Klöppel M; Mulder H; De Vries R; De Zwart M; Timmerman P Blood Stability Testing: European Bioanalysis Forum View on Current Challenges for Regulated Bioanalysis. Bioanalysis 2011, 3 (12), 1333–1336. 10.4155/bio.11.121. [PubMed: 21679027]

(57). Sugihara K; Kitamura S; Ohta S; Tatsumi K Reduction of Hydroxamic Acids to the Corresponding Amides Catalyzed by Rabbit Blood. Xenobiotica 2000, 30 (5), 457–467. 10.1080/004982500237479. [PubMed: 10875680]

(58). Hermant P; Bosc D; Piveteau C; Gealageas R; Lam B; Ronco C; Roignant M; Tolojanahary H; Jean L; Renard PY; et al. Controlling Plasma Stability of Hydroxamic Acids: A MedChem Toolbox. Journal of Medicinal Chemistry 2017, 60 (21), 9067–9089. 10.1021/acs.jmedchem.7b01444. [PubMed: 28985084]

(59). Flipo M; Charton J; Hocine A; Dassonneville S; Deprez B; Deprez-Poulain R Hydroxamates: Relationships between Structure and Plasma Stability. Journal of Medicinal Chemistry 2009, 52 (21), 6790–6802. 10.1021/jm900648x. [PubMed: 19821586]

(60). M.S. G; G. S; J. S; D. J; B. L; P. C; J. C; Y. LB; R.D. H A Phase 1b Study of the Safety, Pharmacokinetics, and Preliminary Antitumor Activity of Citarinostat (ACY-241) in Combination with Paclitaxel (Pac) in Patients (Pts) with Advanced Solid Tumors (AST). Journal of Clinical Oncology 2018. https://doi.org/10.1200/JCO.2018.36.15_suppl.2547 LK - https://doi.org/10.1200/JCO.2018.36.15_suppl.2547http://sfx.library.uu.nl/utrecht?sid=EMBASE&issn=15277755&id=doi:10.1200%2FJCO.2018.36.15_suppl.2547&atitle=A+phase+1b+study+of+the+safety%2C+pharmacokinetics%2C+and+preliminary+antitumor+activity+of+citarinostat+%28ACY-241%29+in+combination+with+paclitaxel+%28Pac%29+in+patients+%28pts%29+with+advanced+solid+tumors+%28AST%29&stitle=J.+Clin.+Oncol.&title=Journal+of+Clinical+Oncology&volume=36&issue=15&spage=&epage=&aulast=Gordon&aufirst=Michael+S.&auinit=M LK - http://sfx.library.uu.nl/utrecht?sid=EMBASE&issn=15277755&id=doi:10.1200%2FJCO.2018.36.15_suppl.2547&atitle=A+phase+1b+study+of+the+safety%2C+pharmacokinetics%2C+and+preliminary+antitumor+activity+of+citarinostat+%28ACY-241%29+in+combination+with+paclitaxel+%28Pac%29+in+patients+%28pts%29+with+advanced+solid+tumors+%28AST%29&stitle=J.+Clin.+Oncol.&title=Journal+of+Clinical+Oncology&volume=36&issue=15&spage=&epage=&aulast=Gordon&aufirst=Michael+S.&auinit=M .

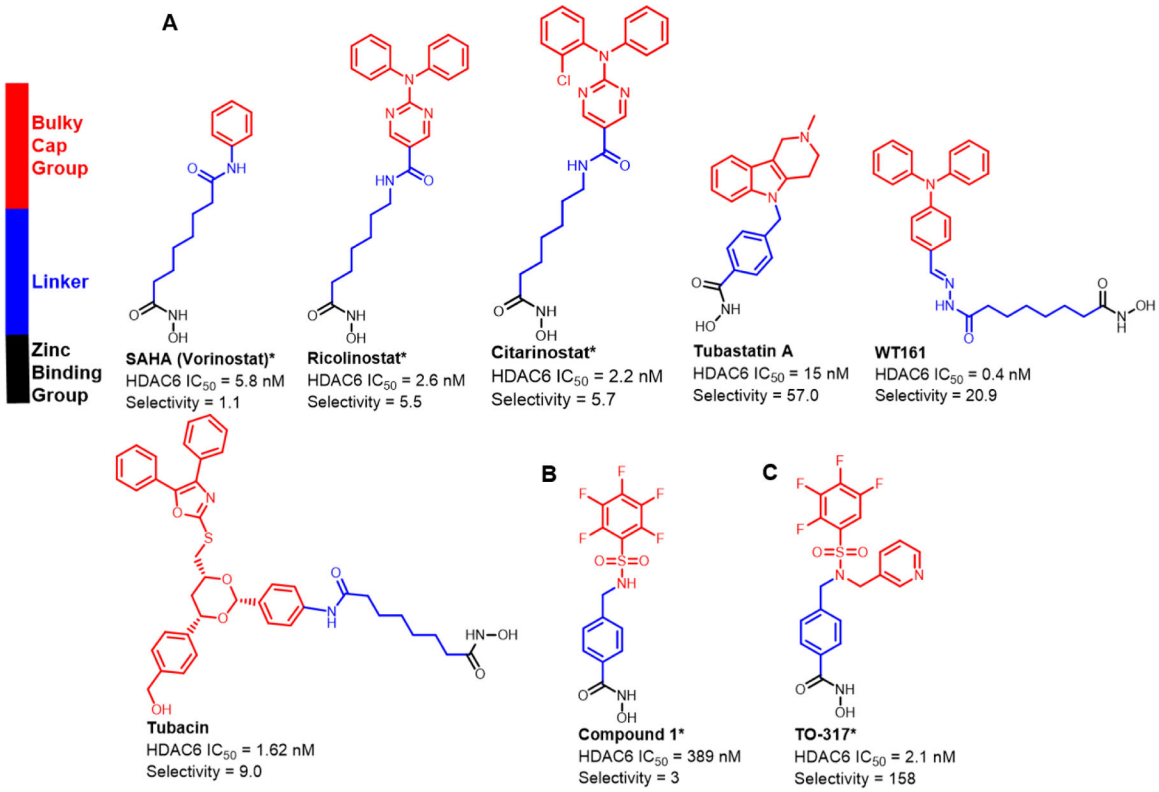

Figure 1:

Currently known HDAC6 inhibitors. The structural features involve a hydroxamic acid which is required for Zn^{2+} binding, and a linker that connects the hydroxamic acid to a cap group. **a)** Currently known inhibitors achieved HDAC6 selectivity by replacing the benzene substituent on SAHA with a bulkier, usually hydrophobic cap group. **b)** Previous studies showed compound **1** is a nM inhibitor against HDAC6 exhibiting limited selectivity c) Current studies show **TO-317** adopts a rotatable cap group with two aromatic substituents that occupy the HDAC6 surface facilitating specific residue interactions.

*IC_{50} values were determined using an activity-based electrophoretic mobility shift assay (EMSA) by Nanosyn Inc., USA.

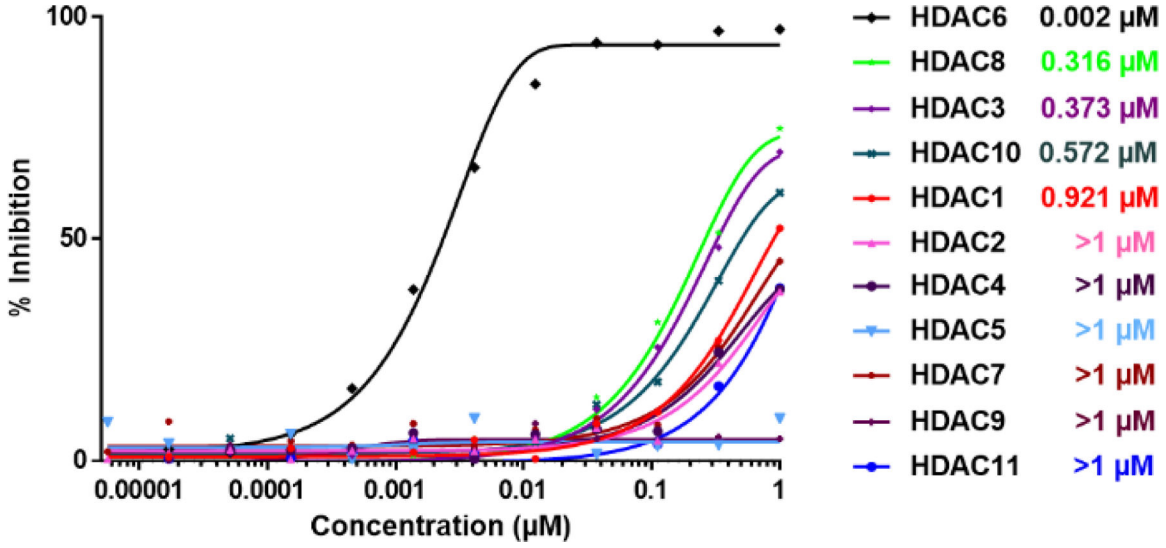

Figure 2:

Overlaid Inhibition curves for **TO-317** against a panel of 11 Zn^{2+}-based HDAC homologs. **TO-317** shows in vitro HDAC6 selectivity across all Zn^{2+}-dependent HDAC homologs and becomes a viable candidate for further biological investigation of the HDAC6 enzyme.

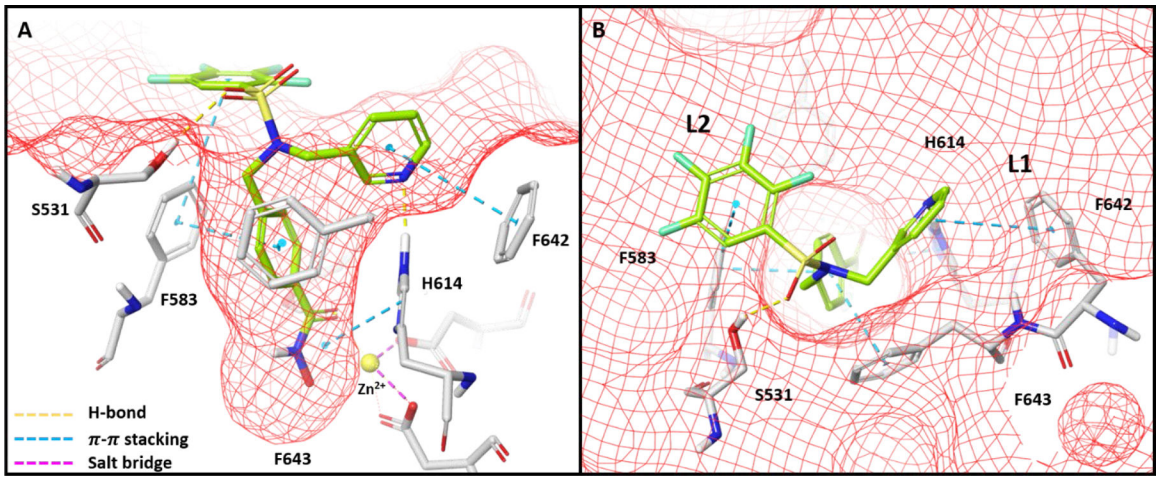

Figure 3:

Docking conformation of **TO-317** with *dr*HDAC6 CD2 (**PDB 5WGI**) reveals occupancy of both L1 and L2 crevices which facilitates a plethora of interactions. Deck A shows the pocket view of these interactions, while deck B shows how **TO-317** adopts a windmill conformation that allows both aromatic ring cap groups to engage with the L1 and L2 crevices of the HDAC6 outer surface.

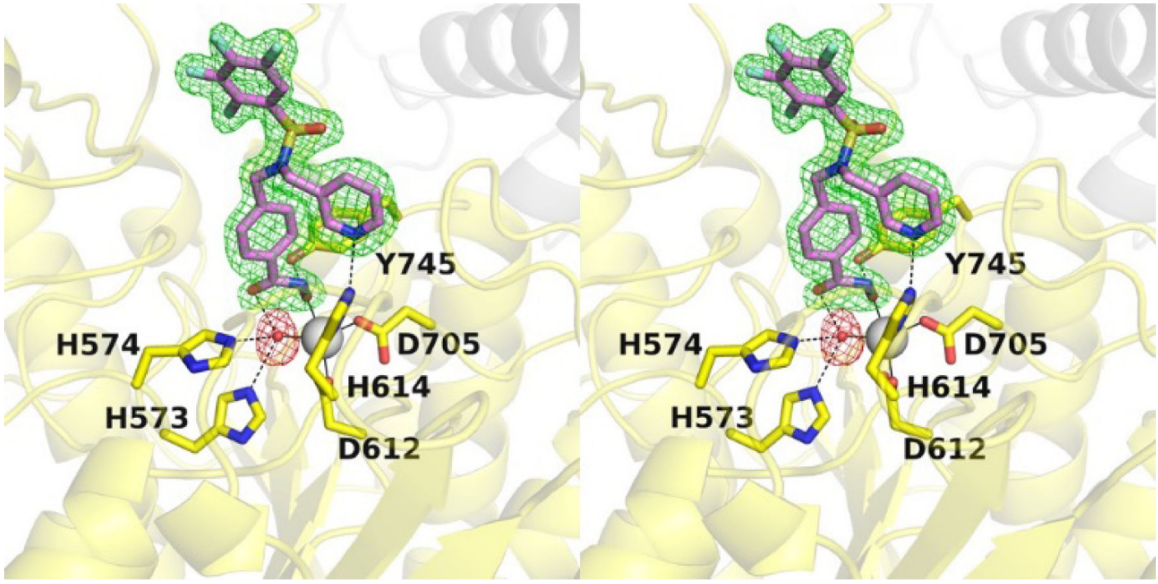

Figure 4.

Stereo-view of a Polder omit map (contoured at 4.0σ) showing the binding of **TO-317** in the active site of HDAC6 (PDB code: **7JOM**). The catalytic Zn^{2+} ion is shown as a grey sphere, the Zn^{2+} bound water molecule is shown as a red sphere; metal coordination and hydrogen bond interactions are shown as solid and dashed black lines, respectively.

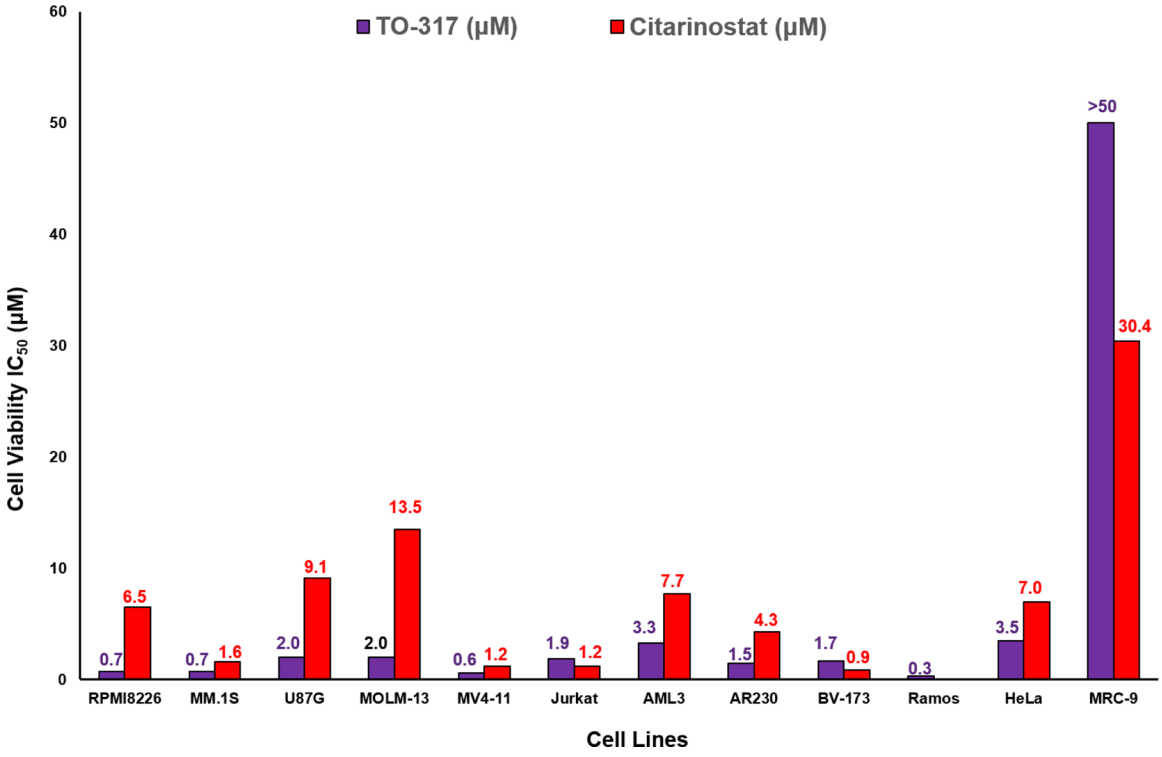

Figure 5:

Cellular potency of **TO-317** and Citarinostat (positive control) in 12 cell lines (1 heathy cell, MRC-9 included). **TO-317** shows anti-proliferative potency across different cancer cells with minimal activity in healthy cells. IC_{50} values are indicated above each graph and reported in μM. IC_{50} values with their 95% confidence intervals are reported in Table S3.

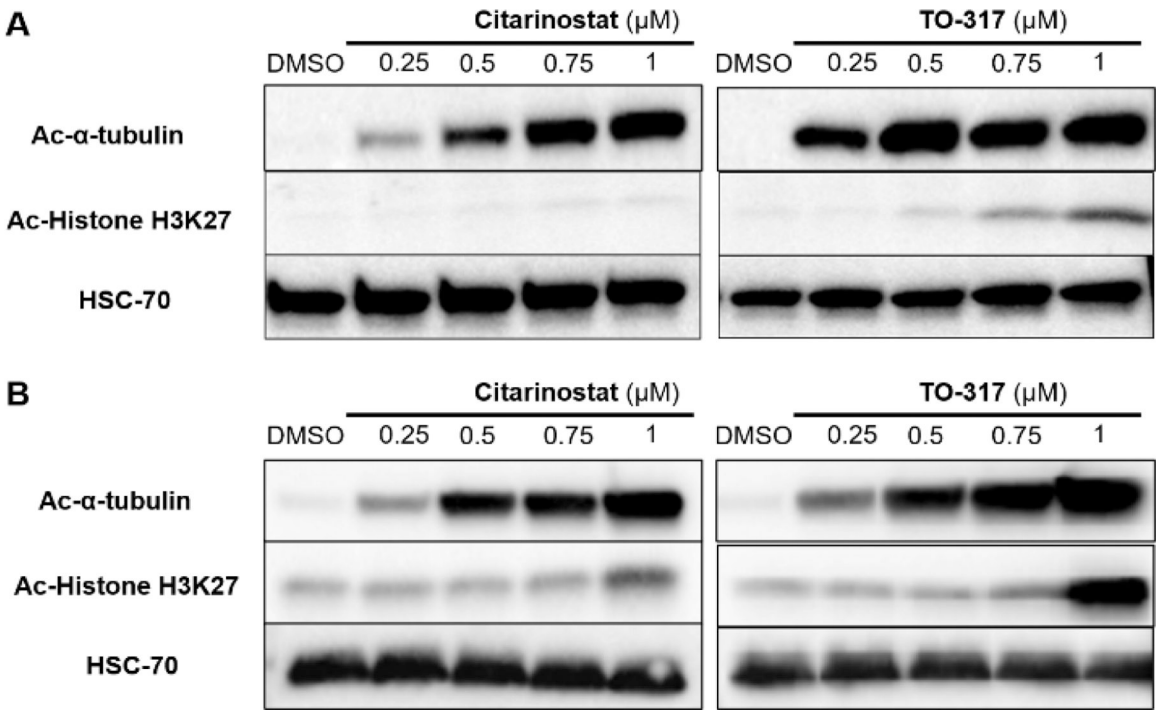

Figure 6:

TO-317 shows superior HDAC6 selectivity and potency in MV4–11 and MM.1S cells. (A) MV4–11 cells treated with increasing doses (0.25 μM - 1 μM) of Citarinostat and **TO-317** show accumulation of Ac-α-tubulin for **TO-317** at 0.25 μM but not for Citarinostat. (B) Similar dose-dependent responses were observed for both inhibitors in MM.1S cells.

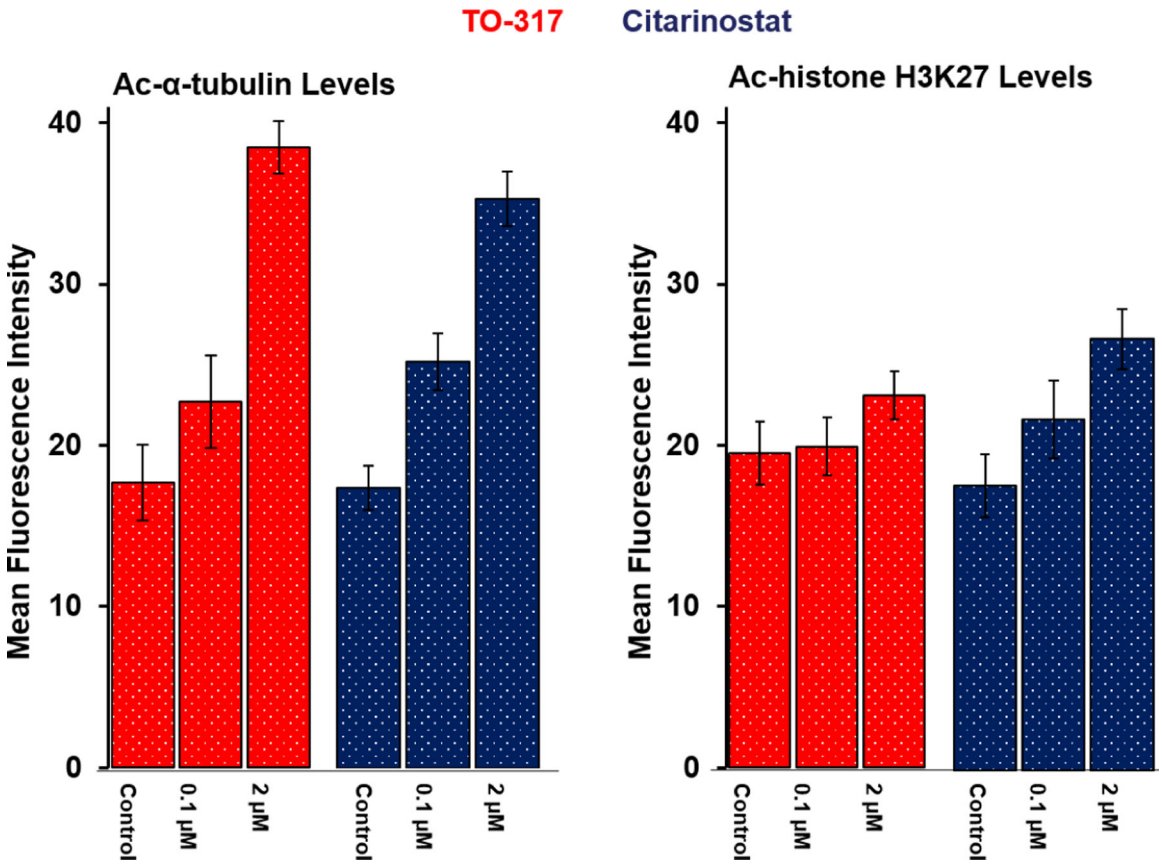

Figure 7:

Quantification of Ac-α-tubulin and Ac-histone levels in immunofluorescence assay. DMSO was used as a negative control in each cohort, and Citarinostat was the positive control. Result indicates that **TO-317** induces a clear dose-dependent increase in acetylated α-tubulin with minimal cellular accumulation of acetylated histones under the same dosing concentrations. Data reported above are an average of duplicate experiments.

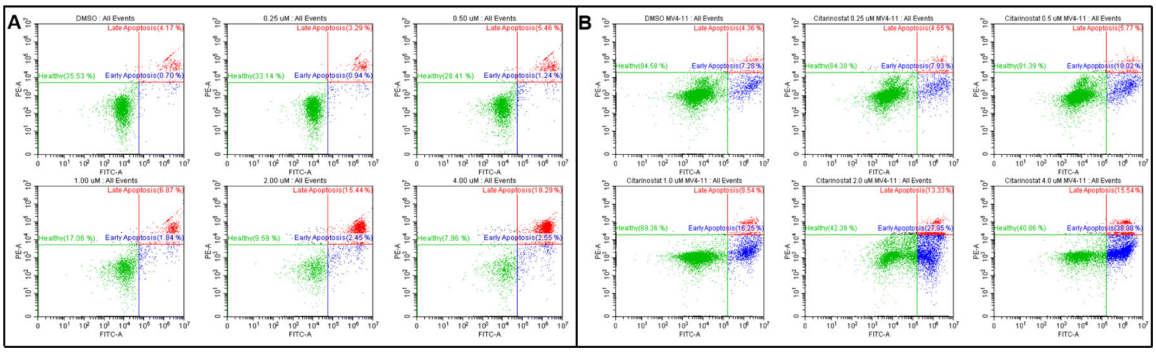

Figure 8:

MV4–11 treated with **TO-317** (Panel A) and Citarinostat (Panel B) leads to dose-dependent programmed cell death. Death by necrosis (Q1) is minimal and consistent at all doses. Dose-dependent cell death by **TO-317** is consistent with a mechanistic approach of cell cycle arrest leading to apoptosis and corroborates the previously observed superior anti-proliferative activity of **TO-317** over Citarinostat, the positive control. Data reported above are an average of duplicate experiments, and quantification of each cell population with the associated standard deviation is reported graphically in Fig. S8-A **&** Fig. S8-B.

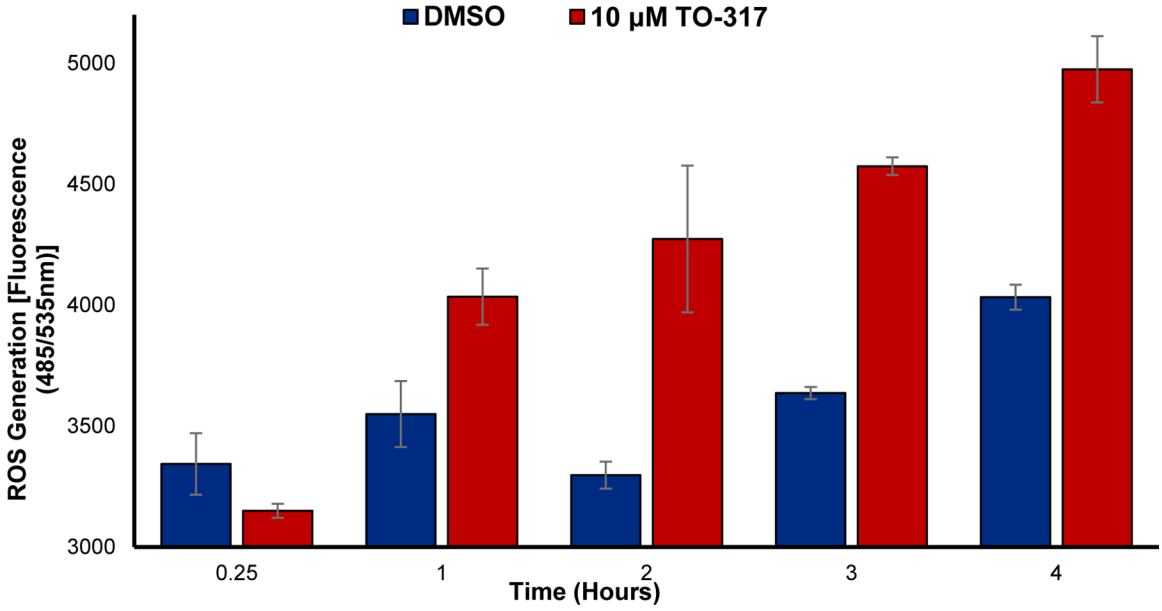

Figure 9:

ROS generation in MV4–11 following incubation with 10 μM **TO-317** for up to 4 h. **TO-317** shows markedly increased levels of ROS after 2 h incubation which continues to increase up to the 4 h incubation time tested. Data reported is an average of duplicate studies.

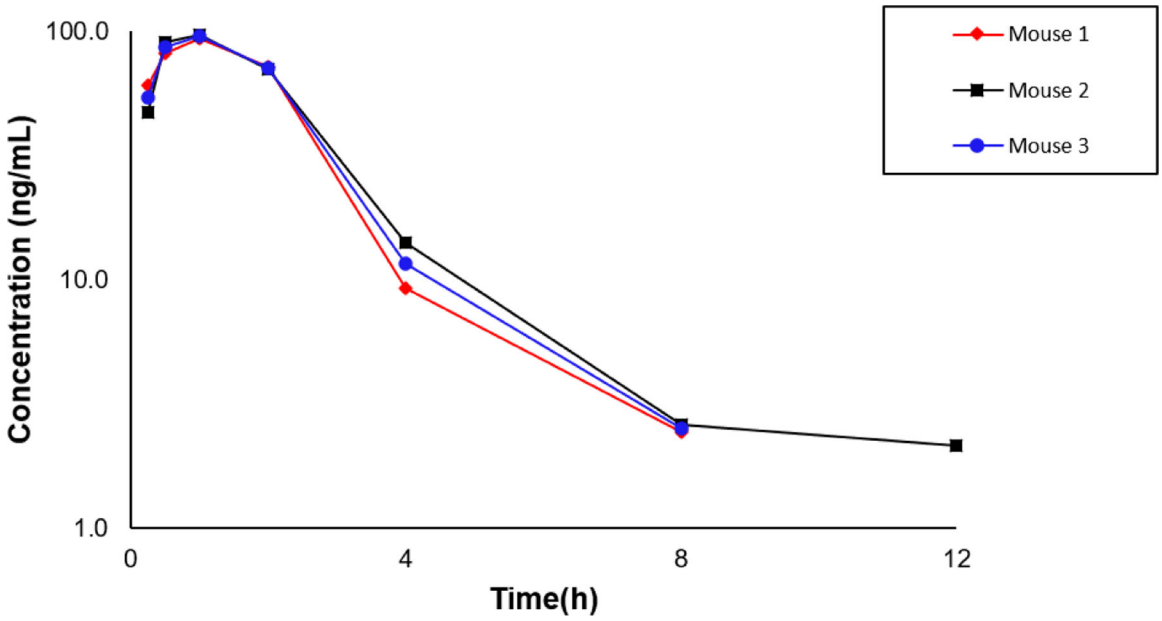

Figure 10:

TO-317 is stable *in vivo* with a $t_{1/2\ (avg)}$ = 1.7 h. Male BALB/c mice were dosed **TO-317** intraperitoneally (50 mg/mL solution 5% DMSO, 30% PEG400, 1% Tween80 & 64% saline) and peaks were detected and quantified from collected blood samples at different time concentrations using a triple-quad LC-MS/MS.

Table 1:

Activity of **1** and derivatives against 4 HDAC homologs. IC_{50} values were determined by EMSA using full-length hHDAC6 and a 6-carboxy fluorescein-aminohexyl amidite (FAM) labeled acetylated peptide substrate of HDAC6 catalytic domain 2. IC_{50} values are an average of duplicate experiments and are reported in μM, and the 95% confidence interval is italicized and reported in brackets close to the IC_{50} values. Sigmoidal curves of inhibitor concentration (12 concentrations, 5.6×10^{-6} μM – 1 μM) vs % inhibition was fitted using XLDB software (a four-parameter sigmoidal dose–response model). Full protocol is described in detail in the supplementary procedure. Full IC_{50} curves are shown in supplementary data.

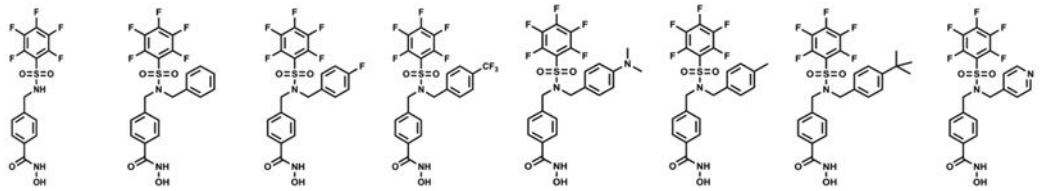

ID	1	2	3	4	5	6	7	8
HDAC3 (μM)	>1	>1	>1	>1	>1	>1	>1	>1
HDAC6 (μM)	0.389	0.009 *(0.0025)*	0.013 *(0.0022)*	0.045 *(0.0160)*	0.029 *(0.0064)*	0.006 *(0.0006)*	0.042 *(0.0240)*	0.014 *(0.0015)*
HDAC8 (μM)	>1	0.150 *(0.0590)*	0.367 *(0.0880)*	>1	>1	0.101 *(0.0032)*	0.068 *(0.1300)*	>1
HDAC11 (μM)	>1	0.122 *(0.1700)*	0.787 *(0.1000)*	>1	>1	0.073 *(0.0540)*	0.088 *(0.0590)*	>1
Selectivity	>3	14	28	>22	>33	12	2	>71

Table 2:

Focused SAR highlights the substitution of the PFB ring with TFB analogs showing improvements in selectivity for HDAC6. We have also shown that TFB analogs have superior metabolic profiles compared to their PFB isotypes. Substituent location on the cap group aromatic ring plays a significant role in targeted HDAC6 binding. The pyridine motifs displayed the most potent and discriminative activity against HDAC6. IC_{50} values were determined as described in Table 1 caption and supplementary procedures. IC_{50} values are an average of duplicate experiments and are reported in μM, and their 95% confidence interval is italicized and reported in brackets under each IC_{50} value. Full IC_{50} curves are shown in supplementary data.

	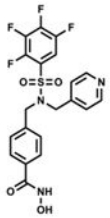	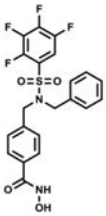	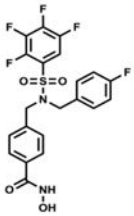	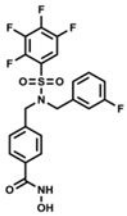	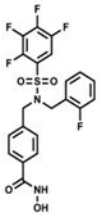	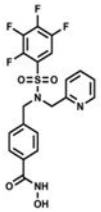	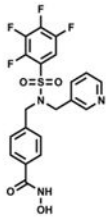
ID	**9**	**10**	**11**	**12**	**13**	**14**	**15 (TO-317)**
HDAC3 (μM)	>1	0.697 *(0.1500)*	>1	>1	>1	0.896 *(0.1500)*	0.373 *(0.0690)*
HDAC6 (μM)	0.011 *(0.0008)*	0.005 *(0.0015)*	0.021 *(0.0060)*	0.014 *(0.0015)*	0.010 *(0.0010)*	0.006 *(0.0017)*	0.002 *(0.0002)*
HDAC8 (μM)	0.581 *(0.0970)*	0.155 *(0.0560)*	0.860 *(0.2600)*	0.412 *(0.1000)*	0.241 *(0.0320)*	0.332 *(0.0980)*	0.316 *(0.0560)*
HDAC11 (μM)	0.472 *(0.1500)*	0.115 *(0.0240)*	>1	0.235 *(0.0740)*	0.263 *(0.0530)*	0.941 *(1.5000)*	>1
Selectivity	**43**	**23**	**41**	**17**	**24**	**55**	**158**

Table 3:

IC_{50} values for **TO-317** against all HDAC isoforms determined with a top concentration of 10 μM. **TO-317** maintains strong *in vitro* inhibitory preference for HDAC6 indicating a promising selectivity profile that is worthy of further biological characterization. IC_{50} values are an average of duplicate experiments, and their 95% confidence interval is italicized and in brackets under each IC_{50} value.

ID	HDAC1	HDAC2	HDAC3	HDAC4	HDAC5	HDAC6	HDAC7	HDAC8	HDAC9	HDAC10	HDAC11
TO-317 IC_{50}	0.921 *(0.1400)*	4.970 *(0.8000)*	0.373 *(0.0690)*	>10	8.650 *(1.5200)*	0.002 *(0.0002)*	7.290 *(1.4100)*	0.316 *(0.0560)*	2.750 *(0.6000)*	0.572 *(0.1400)*	4.870 *(2.2200)*

Table 4:

TO-317 showed extended lifetimes in both mouse plasma and pooled human blood stability assays. Assay values reported was an average of triplicate studies.

	Remaining Percentage TO-317 Concentration				
Assay	**0 min**	**15 min**	**30 min**	**60 min**	**$T_{1/2}$ (min)**
Mouse Plasma*	100%	88.1%	79.8.0%	68.0%	110
Human Whole Blood*	100%	88.0%	80.8%	68.9%	108